Efficient Electrocatalytic Oxygen Evolution on Amorphous Nickel–Cobalt Binary Oxide Nanoporous Layers

Yang Yang,[†,‡,⊥] Huilong Fei,[†,⊥] Gedeng Ruan,[†] Changsheng Xiang,[†] and James M. Tour[†,‡,§,*]

[†]Department of Chemistry, [‡]Smalley Institute for Nanoscale Science and Technology, and [§]Department of Materials Science and NanoEngineering, Rice University, 6100 Main Street, Houston, Texas 77005, United States. [⊥]Y. Yang and H. Fei contributed equally to this work.

ABSTRACT Nanoporous Ni–Co binary oxide layers were electrochemically fabricated by deposition followed by anodization, which produced an amorphous layered structure that could act as an efficient electrocatalyst for water oxidation. The highly porous morphologies produced higher electrochemically active surface areas, while the amorphous structure supplied abundant defect sites for oxygen evolution. These Ni-rich (10–40 atom % Co) binary oxides have an increased active surface area (roughness factor up to 17), reduced charge transfer resistance, lowered overpotential (~325 mV) that produced a 10 mA cm^{-2} current density, and a decreased Tafel slope (~39 mV $decade^{-1}$). The present technique has a wide range of applications for the preparation of other binary or multiple-metals or metal oxides nanoporous films. Fabrication of nanoporous materials using this method could provide products useful for renewable energy production and storage applications.

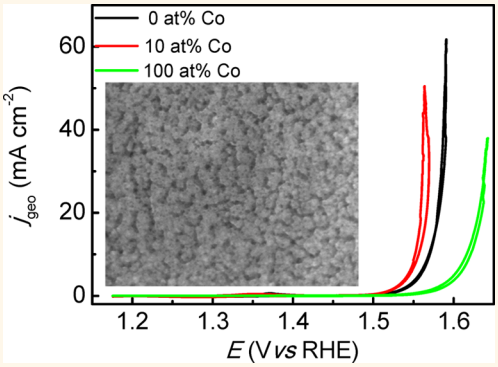

KEYWORDS: electrocatalytic oxygen evolution · nickel–cobalt alloy · binary oxides · amorphous · nanoporous

Primarily because of the sluggish kinetics induced by multistep proton-coupled electron transfer, the electrocatalytic oxygen evolution reaction (OER) for water oxidation is a low- efficiency process. As such, it is unattractive for use in renewable energy production approaches such as photocatalytic or electrolytic water splitting, solar fuel cells and rechargeable metal–air batteries.[1,2] An effective electrocatalyst requires a small Tafel slope (the slope of the linear portion of the potential *vs* the log of the current density) and reduced overpotential (the difference between the theoretical OER potential, 1.23 V *vs* RHE, and the actual potential) to expedite the reaction and enhance the energy conversion efficiency.[3,4] To date, RuO_2 and IrO_2 are considered to be the most efficient catalysts for the OER, but the scarcity of those metals limits their practical usefulness in mass production.[5,6] Therefore, extensive studies have been carried out for the development of inexpensive and efficient OER electrocatalysts based on earth-abundant metals.[7–9] Recently, first-row transition metal oxides, particularly those with Co-based spinel and perovskite structures, such as Co_3O_4 and $(Ln_{0.5}Ba_{0.5})CoO_{3-\delta}$ (Ln = Pr, Sm, Gd and Ho), *etc.*,[10,11] have been widely investigated as efficient OER electrocatalysts due to their excellent electrocatalytic activities.[12] To further enhance the OER electrocatalytic activities of those oxides, modification of both the physical (roughness factor, conductivity, and active site density) and chemical (average oxidation state) properties of the materials have been investigated. This was done through doping or the fabrication of binary oxide mixtures,[13] or increasing the electrochemically active surface areas by forming defined nanostructures (nanorods or macroporous materials) into thin films.[14] Lattice distortion of the surface of amorphous metal oxides was also reported to play a crucial role in reducing the OER activation energy; amorphous oxides had better OER activities than their

* Address correspondence to tour@rice.edu.

Received for review July 9, 2014 and accepted August 18, 2014.

Published online August 18, 2014
10.1021/nn503760c

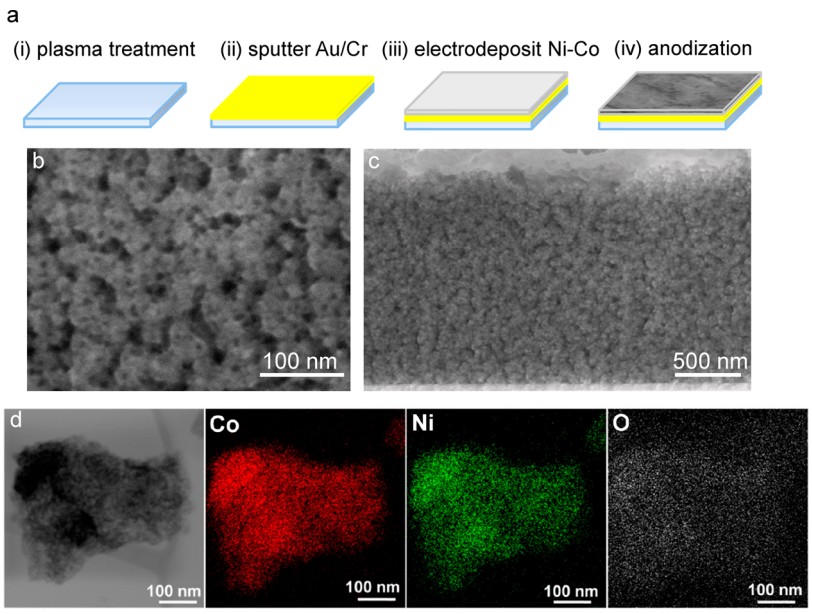

Figure 1. Fabrication process and electron micrographs of the Ni−Co binary oxide NPL: (a) schematic illustration outlining NPL fabrication; (b and c) surface and cross-sectional images of NPL (10 atom % Co); (d) TEM image of NPL and corresponding elemental maps of Co, Ni, and O.

crystalline counterparts.[15] Compared to other conventionally used fabrication techniques, electrodeposition is widely recognized as a practical method to fabricate films and nanostructured materials because it can be used to deposit metal, metal oxides and multimetal alloy layers.[16] And the crystallinity of the deposited layers can be controlled from amorphous to highly crystalline by tailoring the deposition conditions.[17] In addition, most electrodeposition experiments are conducted in ambient conditions at room temperature[18] and no postannealing is needed to remove or decompose organic precursors, as used in, for example, the sol−gel method.[19] However, the drawback of these electrodeposition methods is that they cannot form nanoscale highly porous metal oxides with large amounts of electrochemically active sites without the use of templates.[20] Only recently has the anodic formation of porous Co and Ni compounds been reported,[21,22] and the formation of nanoporous Ni−Co binary oxides is still a challenge due to the different etching kinetics for each metal during anodization.

Here we present a modified technique by using electrodeposition followed by anodization to fabricate amorphous Ni−Co binary oxide layers with highly porous morphologies. The fabricated porous layers are additive-free without requiring any conductive porous carbon materials that could decay at a certain anodic potential. We also investigate the impact of binary oxide compositions on their physical and chemical surface characteristics and electrocatalytic OER performances.

RESULTS AND DISCUSSION

The procedure to fabricate an amorphous Ni−Co binary oxide nanoporous layer (NPL) is schematically shown in Figure 1 along with the microscopic characterization data: (i) plasma-treated commercial glass slides were used as substrates followed by (ii) sputtering 10 nm of chromium and then 50 nm gold as a conductive layer and then (iii) Ni−Co alloy layers with thickness ~1.5 μm (Supporting Information Figure S1) were electrodeposited by using $NiSO_4$ and $CoSO_4$ as Ni and Co sources, respectively, with different molar ratios. Finally, (iv) anodic galvanostatic treatments of the alloy layers were performed to form the amorphous NPL. Electrolytes with different compositions (based on the atomic ratio of Co in the baths from 0 to 100 atom %) were used to electrodeposit Ni−Co alloy layers (see Experimental Section for details). After anodization, morphology changes were observed in the SEM images (Figure 1b and Supporting Information Figure S2) that show <10 nm pores in lower Co content NPL (0 to 40 atom % Co in baths), whereas larger pores with size >50 nm diameters are formed in higher Co content NPL (60 to 100 atom % Co in baths). From the cross-sectional SEM images (Figure 1c and Supporting Information Figure S1b−d), the smooth surface of the as-deposited alloy layers turn into a rough surface throughout the length of the layer indicating that the entire layer is nanoporous after anodization. TEM images revealed no lattice fringes from oxides (Supporting Information Figure S3), which indicates the desired amorphous feature of the NPL. Moreover, TEM elemental mapping performed on the Ni−Co binary oxides NPL (Figure 1d) indicates a uniform distribution of Ni, Co and O throughout the NPL. The compositions of the metal elements in the obtained binary oxides NPL were investigated by X-ray photoelectron spectroscopy (XPS) (Supporting Information

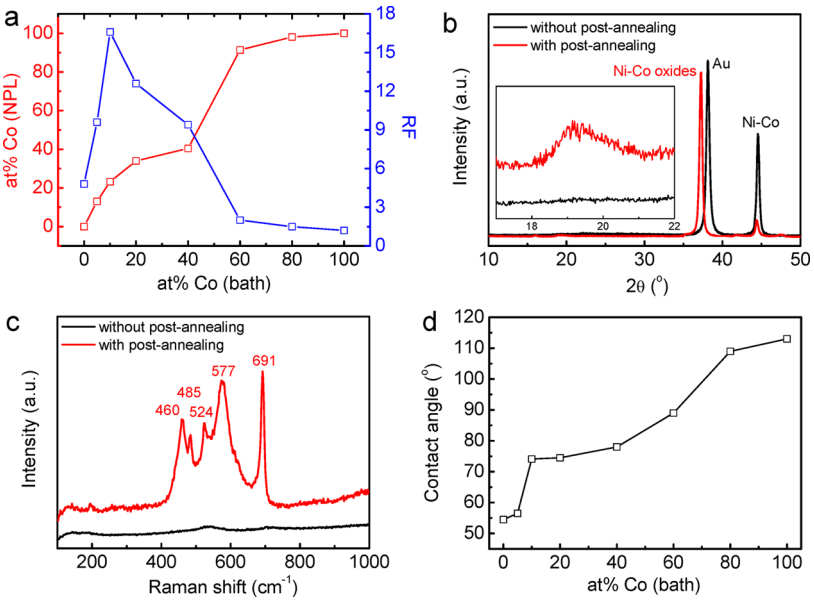

Figure 2. Analysis of the NPL. (a) The variation of Co-content in the NPL and roughness factor on Co-content in the bath. (b and c) XRD patterns and Raman spectra of the Ni−Co binary oxide NPL before and after postannealing at 400 °C for 1 h. The inset in (b) shows the enlarged region in low diffraction angle. (d) The variation of contact angle on the Co-content in bath.

Figure S4) and the correspondence between Co/Ni compositions in the baths and NPL is shown in Figure 2a (unless otherwise specified, the atom % Co in the baths was used to denote the different samples in this paper). The Co content in the NPL did not increase linearly with Co concentration in the baths. A sudden increase was observed over 40 atom % Co in the baths. This is likely due to the faster deposition rate of Co than Ni at specified electrodeposition bath conditions.[23] Because of the different Co and Ni anodic etching kinetics, much smaller pores were formed in Ni or Ni-rich alloys.[24]

The amorphous characteristic of the NPL was also confirmed by XRD (Figure 2b) and Raman analyses (Figure 2c). It is evident that the as-prepared NPL shows no X-ray diffraction peaks for crystalline Ni−Co oxides and the only strong peaks are from sputtered Au and deposited Ni−Co alloy. However, after annealing at 400 °C for 1 h in air, crystalline Ni−Co oxides were formed. Similarly, apparent vibration modes from NiO at 460 and 577 cm^{-1} and Co_3O_4 at 485, 524, and 691 cm^{-1} were found in the postannealed sample.[25,26]

It is important to investigate the interrelationship between the compositions of the Ni−Co binary oxide NPL and their surface characteristics such as the roughness factor, defined as the ratio of the electrochemically active surface area (EASA) to the geometric surface area, and the contact angle, since electrocatalytic processes generally occur on the surface of the catalysts.[27] Although no significant change in the pore size is observed within Ni-rich (0−40 atom % Co) NPL, the roughness factor shows a nonlinear change with increasing Co-content and a maximum value ~17 is achieved at 10 atom % Co sample (Figure 2a). Another interesting result is that with larger pores in the Co-rich NPL (60−100 atom % Co), the roughness factor drops dramatically. This could be affected by multiple factors such as the poor conductivity of Co_3O_4 in the binary oxides, pore size change and hydrophobicity.[28] Moreover, the NPL changes from a hydrophobic to a hydrophilic surface by contact angle measurements (Figure 2d and Supporting Information Figure S5) with the increase of Ni-content in the binary oxides. This can be explained by the fact that the Ni-rich NPL tends to form more hydrated surfaces as detected by XPS (Supporting Information Figure S4).

Electrocatalytic OER activity and kinetics were examined through testing cyclic voltammograms (CVs), polarization curves and electrochemical impedance spectroscopy (EIS) in O_2-saturated 1 M aqueous NaOH with a stationary NPL as the working electrode and Hg/HgO (in 1 M NaOH) as the reference electrode. The representative *iR*-corrected CVs and polarization curves performed at a scan rate of 5 mV s^{-1} are shown in Figure 3a,b (for more details see Supporting Information Figure S6). A significantly reduced onset potential for OER is observed in the Ni-rich NPL (10 atom % Co) compared to both pure NiO and Co_3O_4 due to the greatly increased roughness factor of the NPL.[29] The Ni-rich NPL (10 atom % Co) shows an enhanced OER activity with higher OER current at lower overpotential (η). Mechanistic insights into OER processes are accessible through approximating Tafel slopes from polarization curves. Different Tafel slopes derived at small η were identified from pure NiO (42 mV $decade^{-1}$) and Co_3O_4 (69 mV $decade^{-1}$) NPL, which imply different rate-determining steps in NiO and Co_3O_4 NPL within a given pathway.[30] For Ni-rich NPL (10 atom % Co), the Tafel slope can be reduced to 39 mV $decade^{-1}$

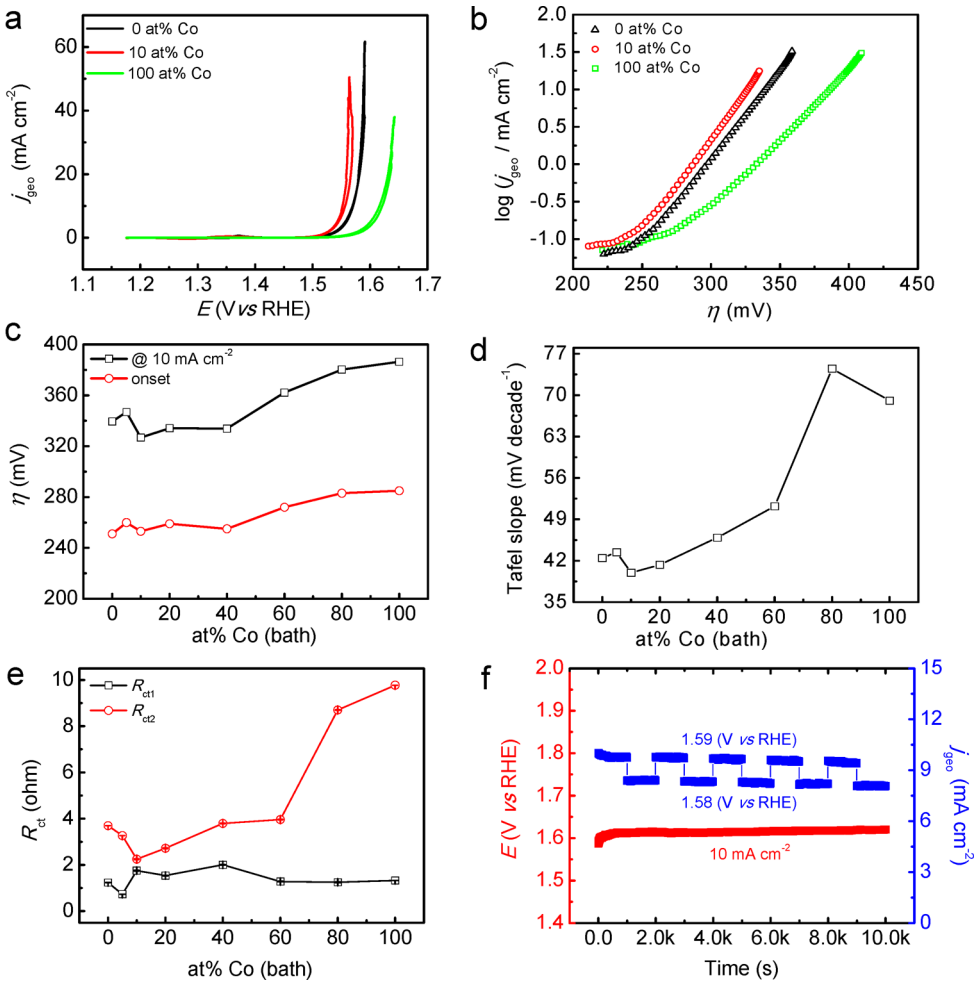

Figure 3. Electrocatalytic OER performance of the Ni−Co binary oxide NPL. (a and b) *iR*-corrected CVs and Tafel plots of the Ni−Co binary oxide NPL (0, 10, and 100 atom % Co) measured at a scan rate of 5 mV s^{-1}, respectively. (c and d) The variation of onset potential/overpotential at 10 mA cm^{-2} and Tafel slope on Co-content in the bath, respectively. (e) The variation of charge transfer resistance on Co-content in the bath. The resistances were simulated from EIS measured at $\eta \sim 350$ mV. (f) Long-term stability tests measured both galvanostatically at 10 mA cm^{-2} and potentiostatically at 1.58/1.59 V *vs* RHE for a total of 20K seconds on the sample electrode. Specific current density (j_{geo}) is normalized to the geometrical area of the electrode.

(with a reaction order ~3/2), which is among the lowest values reported for group VIIIB metal (Fe, Co and Ni) oxides.[31−33] Although the reasons for the differences in the rate-determining steps for different first-row transition metal oxides are controversial,[34] the most likely possibility in this case is due to their different propensities to form hydrated surfaces and the adsorption capacity of OH^-.[35]

The variation of onset potentials determined from the inflection points of the polarization curves, with η at 10 mA cm^{-2}, and the Tafel slopes over Co-content of the baths are shown in Figure 3c,d. The data in Figure 3c demonstrates that the Ni-rich NPL (10 to 40 atom % Co) have apparently reduced η (325 to 335 mV) to get 10 mA cm^{-2} as well as maintaining turn-on η in a low range (250−260 mV). In Figure 3d, the Ni-rich NPL (10−40 atom % Co) have similar Tafel slopes (from 39 to 45 mV decade^{-1}), which indicates the same rate-determining step is responsible for the OER. Electrode kinetics analysis (Figure 3e) was performed by simulating the charge transfer resistance, R_{ct1} for the surface oxide layer and R_{ct2} for the inner oxide layer,[36] from EIS tested at oxygen evolution η (350 mV, Supporting Information Figure S7). The simulated R_{ct1} values for NPL with different Co-content show no significant oscillation within a low value range <2 Ω. This indicates that fast charge transfer occurred on the surface of the NPL. R_{ct2} can be markedly reduced with increasing Ni-content, especially for those NPL with 10−40 atom % Co, which is most likely due to the intrinsically poor conductivity of amorphous Co_3O_4 in the binary oxides.

Long-term stability tests (Figure 3f) were performed on the Ni−Co binary oxides NPL both galvanostatically (at 10 mA cm^{-2}) for 10K s and potentiostatically (alternating between 1.58 and 1.59 V *vs* RHE) for another 10K s on the same electrode. The same electrode was tested continuously under galvanostatic and potentiostatic conditions for 20K s. The OER electrocatalytic

activity for the NPL is stable over long-term testing. The slight initial decay observed in the first 10 min is due to the physical adsorption of the generated bubble on the electrode surface, which reduces the active surface for OER.

To demonstrate the advantages of the amorphous/nanoporous structure of the Ni−Co binary oxide layers, control experiments were performed (Supporting Information Figure S8). It is evident that the sputtered Au-substrate has negligible contribution to the high OER current of the NPL. Also, the as-deposited Ni−Co layer without the nanoporous morphology shows much lower OER current compared with the NPL. As recently reported, amorphous metal oxides with abundant surface defects and lattice dislocations show superior OER performance compared to their well-crystalline counterparts, which is also applicable to these Ni−Co binary oxides NPL. The electrochemical approaches used in the present work, electrodeposition and anodization, are well-known for the capability of forming defect-rich amorphous films. The fabricated Ni−Co binary oxides NPL in the present work show favorable kinetics toward OER with a Tafel slope of ~39 mV decade^{-1} as well as a low overpotential of ~325 mV to get 10 mA cm^{-2}. These values are better than most of the recently reported OER electrocatalysts, such as N-doped graphene hydrogel/NiCo double hydroxide (614 mV decade^{-1}) and active MnO_x (120 mV decade^{-1}),[37,38] and can be considered as competitive candidates for water oxidization in base solution (for more detailed comparison, see Supporting Information Table S1).

CONCLUSION

In summary, we demonstrate a practical method by assisting electrodeposition with anodization to fabricate Ni−Co binary oxides layers which offered nanoporous and amorphous features for water oxidization. The nanoporous layers are additive-free without using any conductive porous carbon materials or binder. With tailoring of the Ni-content in the layers, the surface roughness and hydrophilicity were improved and then efficient electrocatalytic performance with a Tafel slope as low as 39 mV decade^{-1} and a small overpotential (325 mV) achieved a 10 mA cm^{-2} current density. This approach of synthesizing porous layers can be useful in fabricating nanoporous materials for numerous fields in renewable energy production and storage.

EXPERIMENTAL SECTION

Fabrication. Commercial microscope slides (75 × 25 × 1 mm^3, 9101-E, Premiere) as substrates were cleaned and degreased by sonication (Cole Parmer, model 08849-00) first in 2-propanol (≥99.7%, Sigma-Aldrich) and then in deionized water. Then, the slides were further cleaned in a Fischione 1020 argon/oxygen plasma cleaner for 2 min under 600 W power. Au (50 nm) was then sputtered on the substrates as the conductive layer using a Denton Desk V Sputter System (Au coating is used to make the glass slide conductive for electrodeposition, but is not necessary when other conductive substrates such as copper foil are used). Electrodeposition was then carried out in an aqueous mixture of 0 to 0.05 M $NiSO_4$ (99%, Sigma-Aldrich), 0 to 0.05 M $CoSO_4$ (99%, Sigma-Aldrich) and 0.5 M H_3BO_3 (99.5%, Sigma-Aldrich) to galvanostatically deposit Ni−Co alloy layers on the substrates at 10 mA for 1 h. Subsequent anodic treatments were performed galvanostatically at 20 mA for 10 min in a solution of 0.2 M NH_4F (98%, Sigma-Aldrich) with 2 M deionized water in ethylene glycol (Fisher Scientific). The samples were then rinsed with deionized water and dried under nitrogen gas flow.

Characterization. A JEOL 6500F scanning electron microscope (SEM) was used to analyze the morphology of the samples. A JEOL 2010 high resolution transmission electron microscope (HRTEM) was used to observe the morphologies and elemental mapping of the samples. Raman spectra were recorded with a Renishaw Raman RE01 scope (Renishaw, Inc.) using a 514 nm excitation argon laser. X-ray diffraction (XRD) analysis was performed by a Rigaku D/Max Ultima II (Rigaku Corporation, Japan) configured with a Cu Kα radiation, graphite monochromator, and scintillation counter. Chemical compositions of the samples were checked by XPS (PHI Quantera XPS, Physical Electronics). An Al anode at 25 W was used as an X-ray source with a pass energy of 26.00 eV, 45° take-off angle, and a 100 μm beam size. A pass energy of 140 eV was used for survey and 26 eV for atomic concentration. Wettability (contact angle) measurements were conducted on a Ramé Hart contact angle goniometer.

Electrochemical Measurement. The nanoporous layer with geometric area ~0.785 cm^2 was directly used as a stationary working electrode. The electrocatalytic OER tests were performed in O_2-saturated 1 M aq NaOH with platinum foil and Hg/HgO (in 1 M NaOH, CH Instruments) electrode as counter and reference electrodes, respectively, within a three-electrode setup. CVs were performed at a scan rate of 5 mV s^{-1} and polarization curves were converted from linear sweep voltammetry (LSV) measured at 5 mV s^{-1}. EIS were carried out at different overpotentials with a frequency range of 10^{-2} to 10^6 Hz with AC signal amplitude of 5 mV. Long-term stability tests were performed on the Ni−Co binary oxide NPLs both galvanostatically (at 10 mA cm^{-2}) and potentiostatically (1.58 and 1.59 V *vs* RHE, due to the limitation of our testing system only alternating potentials were available). The roughness factor was calculated by dividing the double-layer capacitance obtained from EIS at open circuit potential by the value of 40 μF cm^{-2} (average capacitance for metal oxides in 1 M NaOH). The current density was normalized to the geometric area of the layer and the measured potentials *vs* Hg/HgO were converted to a reversible hydrogen electrode (RHE) according to the Nernst equation ($E_{RHE} = E_{Hg/HgO} + 0.0591$ pH $+ 0.098$). All the electrochemical characterizations were carried out with an electrochemical analyzer (CHI 608D, CH Instruments).

Conflict of Interest: The authors declare no competing financial interest.

Acknowledgment. We thank the Peter M. and Ruth L. Nicholas Post-Doctoral Fellowship of the Smalley Institute for Nanoscale Science and Technology for financial support (Y. Yang). Additional funding was provided by the ONR MURI Program (00006766, N00014-09-1-1066), AFOSR MURI program (FA9550-12-1-0035), and AFOSR (FA9550-09-1-0581).

Supporting Information Available: Cross-sectional SEM images and TEM images of the NPL; SEM images, OER performances, and EIS analysis of the NPL with different Co-contents; XPS analysis; optical images of the NPL during wettability (contact angle) measurements; CVs of the deposited layers with

different treatments; roughness factor calculation; table of OER activities of the Ni−Co binary oxide NPL and published electrodes; additional discussions. This material is available free of charge *via* the Internet at http://pubs.acs.org.

REFERENCES AND NOTES

1. Katsounaros, I.; Cherevko, S.; Zeradjanin, A. R.; Mayrhofer, K. J. J. Oxygen Electrochemistry as a Cornerstone for Sustainable Energy Conversion. *Angew. Chem., Int. Ed.* **2014**, *53*, 102.
2. Gray, H. B. Powering the Planet with Solar Fuel. *Nat. Chem.* **2009**, *1*, 112.
3. Kanan, M. W.; Nocera, D. G. *In Situ* Formation of an Oxygen-Evolving Catalyst in Neutral Water Containing Phosphate and Co^{2+}. *Science* **2008**, *321*, 1072.
4. Gong, M.; Li, Y.; Wang, H.; Liang, Y.; Wu, J. Z.; Zhou, J.; Wang, J.; Regier, T.; Wei, F.; Dai, H. An Advanced Ni-Fe Layered Double Hydroxide Electrocatalyst for Water Oxidation. *J. Am. Chem. Soc.* **2013**, *135*, 8452.
5. Walter, M. G.; Warren, E. L.; McKone, J. R.; Boettcher, S. W.; Mi, Q.; Santori, E. A.; Lewis, N. S. Solar Water Splitting Cells. *Chem. Rev.* **2010**, *110*, 6446.
6. Lee, Y.; Suntivich, J.; May, K. J.; Perry, E. E.; Yang, S.-H. Synthesis and Activities of Rutile IrO_2 and RuO_2 Nanoparticles for Oxygen Evolution in Acid and Alkaline Solutions. *J. Phys. Chem. Lett.* **2012**, *3*, 399.
7. Gorlin, Y.; Jaramillo, T. F. A Bifunctional Nonprecious Metal Catalyst for Oxygen Reduction and Water Oxidation. *J. Am. Chem. Soc.* **2010**, *132*, 13612.
8. Suntivich, J.; May, K. J.; Gasteiger, H. A.; Goodenough, J. B.; Yang, S.-H. A Perovskite Oxide Optimized for Oxygen Evolution Catalysis from Molecular Orbital Principles. *Science* **2011**, *334*, 1383.
9. Chen, S.; Qiao, S.-Z. Hierarchically Porous Nitrogen-Doped Graphene-$NiCo_2O_4$ Hybrid Paper as an Advanced Electrocatalytic Water Splitting Material. *ACS Nano* **2013**, *7*, 10190.
10. Trasatti, S. Electrocatalysis in the Anodic Evolution of Oxygen and Chlorine. *Electrochim. Acta* **1984**, *29*, 1503.
11. Grimaud, A.; May, K. J.; Carlton, C. E.; Lee, Y.-L.; Risch, M.; Hong, W. T.; Zhou, J.; Yang, S.-H. Double Perovskites as A Family of Highly Active Catalysts for Oxygen Evolution in Alkaline Solution. *Nat. Commun.* **2013**, *4*, 2439.
12. Lodi, G.; Sivieri, E.; De Battisti, A.; Trasatti, S. Ruthenium Dioxide-Based Film Electrodes. *J. Appl. Electrochem.* **1978**, *8*, 135.
13. Louie, M. W.; Bell, A. T. An Investigation of Thin-Film Ni-Fe Oxide Catalysts for the Electrochemical Evolution of Oxygen. *J. Am. Chem. Soc.* **2013**, *135*, 12329.
14. Li, Y.; Hasin, P.; Wu, Y. $Ni_xCo_{3-x}O_4$ Nanowire Arrays for Electrocatalytic Oxygen Evolution. *Adv. Mater.* **2010**, *22*, 1926.
15. Smith, R. D. L.; Prévot, M. S.; Fagan, R. D.; Zhang, Z.; Sedach, P. A.; Siu, M. K. J.; Trudel, S.; Berlinguette, C. P. Photochemical Route for Accessing Amorphous Metal Oxide Materials for Water Oxidation Catalysis. *Science* **2013**, *340*, 60.
16. Endres, F.; Bukowski, M.; Hempelmann, R. Natter, H. Electrodeposition of Nanocrystalline Metals and Alloys from Ionic Liquids. *Angew. Chem., Int. Ed.* **2003**, *42*, 3428.
17. Yang, Y.; Wang, X.; Sun, C.; Li, L. Photoluminescence of ZnO Nanorod-TiO_2 Nanotube Hybrid Arrays Produced by Electrodeposition. *J. Appl. Phys.* **2009**, *105*, 094304.
18. Yang, Y.; Wang, X.; Sun, C.; Li, L. CeO_2 Nanorod-TiO_2 Nanotube Hybrid Nanostructure. *J. Am. Ceram. Soc.* **2010**, *93*, 2555.
19. Hench, L. L.; West, J. K. The Sol-Gel Process. *Chem. Rev.* **1990**, *90*, 33.
20. Nielsch, K.; Müller, F.; Li, A. P.; Gösele, U. Uniform Nickel Deposition into Ordered Alumina Pores by Pulsed Electrodeposition. *Adv. Mater.* **2000**, *12*, 582.
21. Lee, C. Y.; Lee, K.; Schmuki, P. Anodic Formation of Self-Organized Cobalt Oxide Nanoporous Layers. *Angew. Chem., Int. Ed.* **2013**, *52*, 2077.
22. Yang, Y.; Ruan, G.; Xiang, C.; Wang, G.; Tour, J. M. Flexible Three-Dimensional Nanoporous Metal-Based Energy Devices. *J. Am. Chem. Soc.* **2014**, *136*, 6187.
23. Wang, L.; Gao, Y.; Xue, Q.; Liu, H.; Xu, T. Microstructure and Tribological Properties of Electrodeposited Ni-Co Alloy Deposits. *Appl. Surf. Sci.* **2005**, *242*, 326.
24. Jin, M.; Zhang, G.; Yu, F.; Li, W.; Lu, W.; Huang, H. Sponge-like $Ni(OH)_2$-NiF_2 composite film with excellent electrochemical performance. *Phys. Chem. Chem. Phys.* **2013**, *15*, 1601.
25. Dietz, R. E.; Parisot, G. I.; Meixner, A. E. Infrared Absorption and Raman Scattering by Two-Magnon Processes in NiO. *Phys. Rev. B* **1971**, *4*, 2302.
26. Hadjiev, V. G.; Iliev, M. N.; Vergilov, I. V. The Raman Spectra of Co_3O_4. *J. Phys. C: Solid State Phys.* **1988**, *21*, L199.
27. Watt-Smith, M. J.; Friedrich, J. M.; Rigby, S. P.; Ralph, T. R.; Walsh, F. C. Determination of the Electrochemically Active Surface Area of Pt/C PEM Fuel Cell Electrodes using Different Adsorbates. *J. Phys. D: Appl. Phys.* **2008**, *41*, 174004.
28. Liang, Y.; Li, Y.; Wang, H.; Zhou, J.; Wang, J.; Regier, T.; Dai, H. Co_3O_4 Nanocrystals on Graphene as A Synergistic Catalyst for Oxygen Reduction Reaction. *Nat. Mater.* **2011**, *10*, 780.
29. McCrory, C. C. L.; Jung, S.; Peters, J. C.; Jaramillo, T. F. Benchmarking Heterogeneous Electrocatalysts for the Oxygen Evolution Reaction. *J. Am. Chem. Soc.* **2013**, *135*, 16977.
30. Bediako, D. K.; Surendranath, Y.; Nocera, D. G. Mechanistic Studies of the Oxygen Evolution Reaction Mediated by a Nickel-Borate Thin Film Electrocatalyst. *J. Am. Chem. Soc.* **2013**, *135*, 3662.
31. Singh, J. P.; Singh, N. K.; Singh, R. N. Electrocatalytic Activity of Metal-Substituted Fe_3O_4 Obtained at Low Temperature for O_2 Evolution. *Int. J. Hydrogen Energy* **1999**, *24*, 433.
32. Esswein, J.; McMurdo, M. J.; Ross, P. N.; Bell, A. T.; Tilley, T. D. Size-Dependent Activity of Co_3O_4 Nanoparticle Anodes for Alkaline Water Electrolysis. *J. Phys. Chem. C* **2009**, *113*, 15068.
33. Matsumoto, Y.; Sato, E. Electrocatalytic Properties of Transition Metal Oxides for Oxygen Evolution Reaction. *Mater. Chem. Phys.* **1986**, *14*, 397.
34. Lyons, M. E. G.; Brandon, M. P. The Oxygen Evolution Reaction on Passive Oxide Covered Transition Metal Electrodes in Aqueous Alkaline Solution. Part 1-Nickel. *Int. J. Electrochem. Sci.* **2008**, *3*, 1386.
35. Rolison, D. R.; Hagans, P. L.; Swider, K. E.; Long, J. W. Role of Hydrous Ruthenium Oxide in Pt-Ru Direct Methanol Fuel Cell Anode Electrocatalysts: The Importance of Mixed Electron/Proton Conductivity. *Langmuir* **1999**, *15*, 774.
36. Doyle, R. L.; Lyons, M. E. G. An Electrochemical Impedance Study of the Oxygen Evolution Reaction at Hydrous Iron Oxide in Base. *Phys. Chem. Chem. Phys.* **2013**, *15*, 5224.
37. Chen, S.; Duan, J.; Jaroniec, M.; Qiao, S. Z. Three-Dimensional N-Doped Graphene Hydrogel/NiCo Double Hydroxide Electrocatalysts for Highly Efficient Oxygen Evolution. *Angew. Chem., Int. Ed.* **2013**, *52*, 13567.
38. Indra, A.; Menezes, P. W.; Zaharieva, I.; Baktash, E.; Pfrommer, J.; Schwarze, M.; Dau, H.; Driess, M. Active Mixed-Valent MnO_x Water Oxidation Catalysts through Partial Oxidation (Corrosion) of Nanostructured MnO Particles. *Angew. Chem., Int. Ed.* **2013**, *52*, 13206.